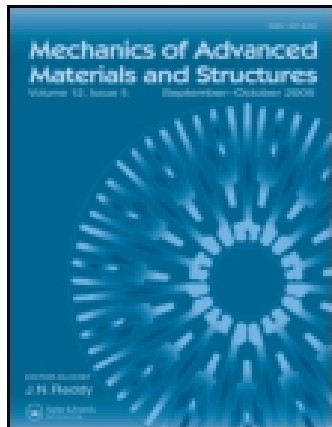


This article was downloaded by: [the LANL Research Library]

On: 09 March 2015, At: 08:19

Publisher: Taylor & Francis

Informa Ltd Registered in England and Wales Registered Number: 1072954 Registered office: Mortimer House, 37-41 Mortimer Street, London W1T 3JH, UK



Mechanics of Advanced Materials and Structures

Publication details, including instructions for authors and subscription information:

<http://www.tandfonline.com/loi/umcm20>

A Resource Allocation Framework for Experiment-Based Validation of Numerical Models

S. Atamturktur^a, J. Hegenderfer^a, B. Williams^b, M. Egeberg^a, R. A. Lebensohn^c & C. Unal^d

^a Glenn Department of Civil Engineering, Clemson University, Clemson, South Carolina, USA

^b CS-Division, Los Alamos National Laboratory, Los Alamos, New Mexico, USA

^c MTS-Division, Los Alamos National Laboratory, Los Alamos, New Mexico, USA

^d D-Division, Los Alamos National Laboratory, Los Alamos, New Mexico, USA

Accepted author version posted online: 30 Jun 2014.



CrossMark

[Click for updates](#)

To cite this article: S. Atamturktur, J. Hegenderfer, B. Williams, M. Egeberg, R. A. Lebensohn & C. Unal (2015) A Resource Allocation Framework for Experiment-Based Validation of Numerical Models, *Mechanics of Advanced Materials and Structures*, 22:8, 641-654, DOI: [10.1080/15376494.2013.828819](https://doi.org/10.1080/15376494.2013.828819)

To link to this article: <http://dx.doi.org/10.1080/15376494.2013.828819>

PLEASE SCROLL DOWN FOR ARTICLE

Taylor & Francis makes every effort to ensure the accuracy of all the information (the "Content") contained in the publications on our platform. However, Taylor & Francis, our agents, and our licensors make no representations or warranties whatsoever as to the accuracy, completeness, or suitability for any purpose of the Content. Any opinions and views expressed in this publication are the opinions and views of the authors, and are not the views of or endorsed by Taylor & Francis. The accuracy of the Content should not be relied upon and should be independently verified with primary sources of information. Taylor and Francis shall not be liable for any losses, actions, claims, proceedings, demands, costs, expenses, damages, and other liabilities whatsoever or howsoever caused arising directly or indirectly in connection with, in relation to or arising out of the use of the Content.

This article may be used for research, teaching, and private study purposes. Any substantial or systematic reproduction, redistribution, reselling, loan, sub-licensing, systematic supply, or distribution in any form to anyone is expressly forbidden. Terms & Conditions of access and use can be found at <http://www.tandfonline.com/page/terms-and-conditions>

A Resource Allocation Framework for Experiment-Based Validation of Numerical Models

S. ATAMTURKTUR¹, J. HEGENDERFER¹, B. WILLIAMS², M. EGEBERG¹, R. A. LEBENSOHN³, and C. UNAL⁴

¹Glenn Department of Civil Engineering, Clemson University, Clemson, South Carolina, USA

²CS-Division, Los Alamos National Laboratory, Los Alamos, New Mexico, USA

³MTS-Division, Los Alamos National Laboratory, Los Alamos, New Mexico, USA

⁴D-Division, Los Alamos National Laboratory, Los Alamos, New Mexico, USA

Received 2 August 2012; accepted 20 November 2012.

In experiment-based validation, uncertainties and systematic biases in model predictions are reduced by either increasing the amount of experimental evidence available for model calibration—thereby mitigating prediction uncertainty—or increasing the rigor in the definition of physics and/or engineering principles—thereby mitigating prediction bias. Hence, decision makers must regularly choose between either allocating resources for experimentation or further code development. The authors propose a decision-making framework to assist in resource allocation strictly from the perspective of predictive maturity and demonstrate the application of this framework on a nontrivial problem of predicting the plastic deformation of polycrystals.

Keywords: Bayesian inference, model calibration, uncertainty quantification, predictive maturity, viscoplastic self-consistent, material plasticity models

1. Introduction

Numerical models are approximate representations of real-world phenomena and, thus, simulations invariably suffer from a degree of inaccuracy and imprecision that can be attributed to: (i) incomplete modeling of physics and/or engineering principles, (ii) imprecisely known model input parameters, and (iii) numerical uncertainties incurred while solving the mathematical equations [1, 2].

Incomplete modeling of physics and/or engineering principles, the first factor, refers to the physical phenomena that are either completely unforeseen or that are known, but too complex to incorporate in the model. This incompleteness invariably causes systematic bias in predictions [3–7] and often leads to missing input parameters [8]. Imprecise model parameters, the second factor, are identified by the analyst; however, their precise values (or distributions) remain unknown [9, 10]. These imprecise model parameters are typically the main contributors to the uncertainty in predictions. Numerical uncertainties, the third factor, can be treated by code and solution verification activities that ensure the mathematical equations are solved correctly [11–13]. Verification is a prerequisite to experiment-based validation [14] and, thus, the third factor, which involves numerical uncertainties, is excluded from the scope of the present article.

The primary aim of the model developer then becomes one of reducing the parameter uncertainty and systematic bias in model predictions. These objectives can be achieved by allocating resources to either (i) undertake *experimentation* to increase the number of physical observations used in the model calibration process or (ii) *code development* to improve the manner in which physics and/or engineering principles are defined. Expanding the experimental campaign by conducting new experiments can reduce parameter uncertainty and produce a more refined estimate of systematic bias, while improvement in the description of physics and/or engineering principles can lead to a reduction in the systematic bias. An improved, more detailed model may, however, lead to a higher number of uncertain input parameters and increase the prediction uncertainty [8]. Thus, reducing prediction uncertainty and prediction bias are often conflicting objectives [15]. Therefore, the relative benefits of these two routes, further experimentation versus further code development, vary depending upon available experimental measurements and the existing predictive capability of the numerical model.

Considering the finite resources, effectively choosing one approach over the other becomes an issue of efficient allocation of available resources. By focusing on the relative benefits of each approach strictly from the perspective of predictive capability, the authors propose a resource allocation framework that aids in the selection between further experimentation and code development. The application of this proposed framework is demonstrated on the viscoplastic self-consistent (VPSC) material code for modeling plastic deformation.

Address correspondence to S. Atamturktur, Glenn Department of Civil Engineering, Clemson University, Lowry Hall, Clemson, SC 29634, USA. E-mail: sez@clemson.edu

2. Resource Allocation Framework

Figure 1 illustrates the proposed framework, which begins with an initial numerical model and a starting set of physical measurements. This initial model is imprecise due to parameter uncertainties and, thus, must be calibrated against experiments. Such calibration is possible using a variety of back-calculation techniques. In this study, a statistical inference procedure originally proposed by Kennedy and O'Hagan [7] and formulated into a standard model calibration procedure by Higdon et al. [5] is adopted. This calibration procedure conditions the probability distributions of input parameters to the experimental evidence reducing the uncertainties in the input parameters, and thus leading to a reduction in prediction uncertainty. An increased availability of experiments results in a greater reduction in prediction uncertainty. In the framework proposed herein, this reduction is traced by quantifying the information gained using an entropy-based metric.

Aside from prediction uncertainty, the initial numerical model in Figure 1 also has a prediction bias, i.e., fundamental inability to reproduce the reality that cannot be remedied solely by calibrating the input parameters. According to Kennedy and O'Hagan [7], prediction bias can be determined by quantifying the deviations between the experiments and the model predictions obtained with 'best fitted' parameter values. Since experiments are only available at discrete settings, empirically training an error model becomes necessary to estimate the systematic bias at the untested settings [5]. As more experiments become available, the prediction bias can be estimated with greater fidelity, ultimately converging to the "true" bias of the model. In the framework proposed herein, the convergence of prediction bias is traced by calculating an averaged bias for the entire domain of applicability through the independently trained empirical error model, henceforth referred to as *discrepancy*.

At the decision node in the framework, the decision maker must assess the predictive capability of the numerical model by evaluating the stabilization of the discrepancy and the information gain metrics throughout the domain of applicability. For a sound model developed based on well-founded physics or engineering principles, the absence of stabilization of the information gain metric indicates that the prediction uncertainty has not yet been fully mitigated, while the absence of stabilization of the discrepancy indicates that prediction bias has not yet been properly defined. In this case, resources must be allocated for experimentation. Poorly built models fail to exhibit stabilization in discrepancy even after a significant number of experiments are conducted; therefore, at this point in the framework, a measure of how well the current experiments explore the domain of applicability (referred to as coverage) is compared to a maximum coverage limit [16–18]. Exceeding the maximum coverage limit without stabilization indicates that the model is too crude for its purposes and resources must be allocated for code development.

If stabilization is observed, however, then the ability of the available experiments to sufficiently explore the domain is analyzed. Stabilization, when only a small portion of the domain is explored by experiments, cannot ensure that the prediction

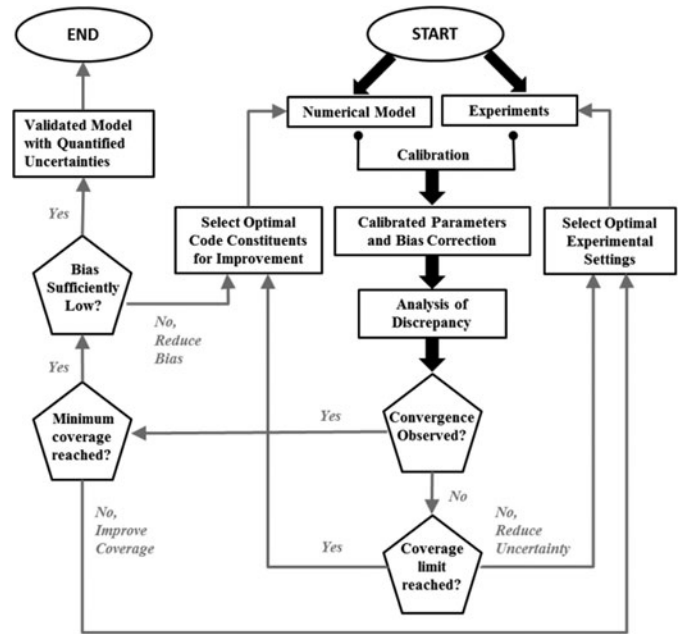


Fig. 1. Predictive capability framework.

bias is properly defined throughout the entire domain. Therefore, a minimum coverage limit needs to be reached; otherwise, more experiments must be conducted to explore the domain of applicability.

If stabilization is observed and the minimum coverage threshold is met, then the epistemic component of parameter uncertainty can be expected to be adequately reduced, and the inferred prediction bias can be considered a proper representation of the incompleteness and inexactness of the model. In this case, further experimentation would only marginally improve the inference of the systematic bias, and allocating resources to experiments cannot be justified. The decision maker must then evaluate if the remaining prediction bias is at an acceptably low level for the application of interest.

If the prediction bias is sufficiently low, the model is considered valid for the particular application. If the prediction bias is unacceptably high for the specific purposes of model predictions, the physics and/or engineering principles in the model must be improved. An improved model may have a larger number of uncertain parameters and may require a more extensive experimental campaign to mitigate the increased prediction uncertainty [8]. Therefore, it becomes necessary to check the stabilization of both information gain metric and discrepancy simultaneously. The framework in Figure 1 therefore loops through the aforementioned steps until the formulated discrepancy and information gain metrics converge to the acceptable levels.

3. Metrics for Prediction Uncertainty and Bias

3.1. Prediction Uncertainty: Information Gain

As the information gain is equal to the amount of uncertainty removed, entropy, defined as a measure of uncertainty,

is equivalent to the amount of information [19]. Herein, an information gain metric based on Shannon entropy is utilized to quantify the prediction uncertainty as additional experiments become available to condition the posterior distributions of input parameters. For a discrete random variable, z , with a probability mass function, $p(z)$, the entropy is expressed as:

$$H(z) = - \sum_{z \in Z} p(z) \log p(z), \quad (1)$$

where the logarithm to base 2 is used to measure entropy in bits and z represents the calibrated model predictions. As an increasing number of experiments are used in the calibration process, the information gain metric, expressed in percentages, is calculated using the following relationship:

$$\text{Info - Gain}(i)(\%) = \left(\frac{H_{ref} - H_{\text{expt}(i)}}{H_{ref}} \right) * 100, \quad (2)$$

where H_{ref} is the entropy calculated for the model predictions obtained with the initial distributions of the calibration parameters prior to the availability of experiments. $H_{\text{expt}(i)}$ is the entropy of the calibrated model predictions, in which i is the number of experiments used in the calibration process.

While the information gain metric is an excellent tool for quantifying the reduction in prediction uncertainty, it does not make any assertions about the prediction bias. Therefore, both the convergence of systematic bias and information gain must be evaluated while discerning the necessity of additional experiments or further code development.

3.2. Prediction Bias: Model Form Error

A multivariate generalization [5, 6] of a model calibration approach formulated by Kennedy and O'Hagan [7] is implemented, in which experiments are exploited to infer uncertain input parameters while simultaneously considering the incompleteness of the model. Here, the experimental observation, $y(x)$, is given by:

$$y(x) = \eta(x, \theta) + \delta(x) + \varepsilon(x), \quad (3)$$

where $\eta(x, \theta)$ denotes the model predictions, $\delta(x)$ represents the estimated systematic bias between reality and the predictions, and $\varepsilon(x)$ denotes the experimental error. Here, x represents settings at which observations are made (i.e., control parameters), and θ denotes the best values for the calibration parameters, t .

For many practical problems, the complexity and computational demands of numerical models limit the number of possible runs. To obtain predictions at untried settings, an inexpensive surrogate (also known as emulator) can be trained as a substitute for the numerical model. Here, a Gaussian process (GP) emulator is used to represent the numerical model predictions, $\eta(x, t)$, which is specified by a mean function, $\mu(x, t)$,

and a covariance function [5]:

$$\begin{aligned} \text{Cov}((x, t), (x', t')) &= \frac{1}{\lambda_\eta} \prod_{k=1}^{p_x} \rho_{\eta k}^{4(x_k - x'_k)^2} \\ &\times \prod_{k=1}^{p_t} (\rho_{\eta k, p_x+k})^{4(t_k - t'_k)^2}, \end{aligned} \quad (4)$$

where λ_η and $\rho_{\eta k}$ vectors are the so-called hyper-parameters for the GP emulator for model predictions, which control the marginal precision of $\eta(x, t)$ and the dependence strength in the components of the x and t directions, respectively. In Eq. (4), p_x and p_t are the number of control and calibration parameters, respectively.

Similarly, for the estimated systematic bias, $\delta(x)$, a GP emulator is employed with a zero mean and a covariance function [5]:

$$\text{Cov}((x, x')) = \frac{1}{\lambda_\delta} \prod_{k=1}^{p_x} \rho_{\delta k}^{4(x_k - x'_k)^2}, \quad (5)$$

where λ_δ and $\rho_{\delta k}$ are hyper-parameters for the GP emulator for prediction bias, which control the marginal precision of $\delta(x)$ and the dependence strength in the components of the x direction, respectively. The hyper-parameters ensure a smooth and differentiable form for both $\eta(x, t)$ and $\delta(x)$.

In the Bayesian calibration framework, the true but unknown values of the calibration parameters, θ , are inferred exploiting the availability of the experimental data, where the existing knowledge about calibration parameters and the hyper-parameters of the GP emulators are incorporated through prior distributions. The posterior distribution conditioned on experimental data is given by:

$$\begin{aligned} \pi(\theta, \mu, \lambda_\eta, \rho_\eta, \lambda_\delta, \rho_\delta | D) &\propto \\ L(D|\theta, \mu, \lambda_\eta, \rho_\eta, \lambda_\delta, \rho_\delta, \sum_y) &\times \pi(\theta) \times \pi(\mu) \times \pi(\lambda_\eta) \\ &\times \pi(\rho_\eta) \times \pi(\lambda_\delta) \times \pi(\rho_\delta), \end{aligned} \quad (6)$$

where D is the joint vector of experimental data and numerical model outputs, $L(D|\theta, \cdot)$ is the likelihood function, \sum_y is the observation covariance matrix, and $\pi(\cdot)$ is the prior distributions (for detailed discussion see Higdon et al. [5]).

A Markov chain Monte Carlo (MCMC) algorithm, specifically Metropolis–Hasting algorithm [20, 21], is used to explore the posterior distributions for both the calibration parameters and the aforementioned hyper-parameters. During the MCMC random walk, calibration parameter values that generate predictions with greater agreement with the experimental data over the domain of applicability are accepted based on the established maximum likelihood criteria [20, 21].

Upon obtaining the hyper-parameters of the GP model, the discrepancy $\delta(x^*)$ can be estimated at untested input settings, x^* throughout the entire domain of applicability. This empirically trained discrepancy model can then be aggregated to obtain an average representation of prediction bias throughout the domain.

Table 1. Stress and texture intensity experimental results for 5182 Al

Experiment	Temperature (°C)	Strain rate (s ⁻¹)	Stress (MPa) @ strain = 0.6	Texture intensity (001)	Texture intensity (101)
A	200	10 ⁻³	226.2	1.00–1.41	4.00–6.00
B	300	10 ⁻³	91.4	0.58–0.71	4.00–6.00
C	350	10 ⁻³	50.0	2.00–2.83	2.83–4.00
D	400	10 ⁻³	30.6	NA	NA
E	500	10 ⁻³	14.9	4.00–6.00	2.00–2.83
F	550	10 ⁻³	7.0	NA	NA
G	200	1	280.0	NA	NA
H	300	1	193.7	NA	NA
I	400	1	121.3	1.41–2.00	4.00–6.00
J	500	1	65.5	2.00–2.83	0.00–0.58
K	550	1	43.0	2.83–4.00	0.58–0.71

4. Viscoplastic Self-Consistent (VPSC) Material Model

Lebensohn and Tomé [22] developed a VPSC material model for modeling the plastic deformation of polycrystals. A polycrystal is modeled by a set of single crystals (grains) with initial crystallographic orientations that represent the initial texture of the aggregate and evolve during plastic deformation. In turn, each grain is treated as an ellipsoidal inclusion with anisotropic viscoplastic properties, deforming in a homogenous equivalent medium that has the *a priori* unknown average properties of the aggregate. This leads to a relation between the strain-rate and stress in each individual grain with the global stress and strain-rate of the aggregate through localization equations. The viscoplastic deformation of the crystals occurs by dislocation motion and can be modeled in terms of constitutive relations between the deviatoric stress and strain-rate tensors. Viscoplastic deformation will occur when a slip system activates and dislocations move under an applied stress. The final deformation is obtained in the VPSC formulation through imposing a macroscopic strain-rate during each incremental deformation step. The strain-rate and stress from each previous step is used as the starting values for the next step. Stress–strain curves and texture development constitute the typical output of a VPSC calculation. Recall that the numerical uncertainty must be verified prior to validation (see Lebensohn et al. [23] for verification of the VPSC code against “exact” full-field formulations).

In the present study, two versions of the VPSC code are utilized: the original glide-only (G) version, used for predictions of plasticity of polycrystals; and the climb-and-glide (C&G) version, with improved physics for the prediction of polycrystal response under creep conditions.

4.1. Glide VPSC

In the G version of the VPSC code, a Schmid-type constitutive behavior is used to describe the dislocation motion in the constituent single-crystals [22]. As such, dislocations lie and move within the slip plane and are activated by shear stresses; their motion can only accommodate simple shear deformation

on this plane. Glide activity in several slip planes is able to accommodate an arbitrary deformation applied to the crystal. The constitutive equation at the single crystal level is expressed as:

$$\dot{\epsilon} = \dot{\gamma}_o \sum_{s=1}^{N_s} m^s \left(\frac{|m^s : \sigma|}{\tau_o^s} \right)^{n_g} \text{sgn}(m^s : \sigma), \quad (7)$$

where σ is the stress applied to the crystal and $\dot{\epsilon}$ is the strain rate, accommodated by glide; m^s and τ_o^s are the Schmid tensor and the critical resolved shear stress associated with glide in the system(s), respectively. The stress exponent, n_g , represents the inverse of rate sensitivity for the glide activity, and $\dot{\gamma}_o$ denotes a normalization factor. The single crystal equation for strain rate is summed over all active slip systems, N_s .

4.2. Climb-and-Glide VPSC

Lebensohn et al.’s [24] constitutive model for aggregates of single crystals deforming by climb and glide is an improvement to the original VPSC approach that considers deformations by glide only. At temperatures below 50% of the melting temperature, glide-controlled creep dominates; however, at higher temperatures, local nonequilibrium concentrations of point defects interacting with dislocations allow for dislocations to climb in addition to glide. Dislocation climb becomes very relevant in high-temperature plasticity and irradiation creep. The direction of dislocation motion is determined by the velocity vector composed of two components: the glide velocity (lies in glide plane) and the climb velocity (normal to the glide plane). The glide component depends upon the shear stress component acting on the glide plane while the climb component depends on the full stress tensor. The extension of Eq. (7) to the C&G case is expressed as:

$$\dot{\epsilon} = \dot{\gamma}_o \sum_{s=1}^{N_s} \left\{ m^s \left(\frac{|m^s : \sigma|}{\tau_o^s} \right)^{n_g} \times \text{sgn}(m^s : \sigma) + c^s \left(\frac{|c^s : \sigma|}{\sigma_o^s} \right)^{n_c} \times \text{sgn}(c^s : \sigma) \right\}, \quad (8)$$

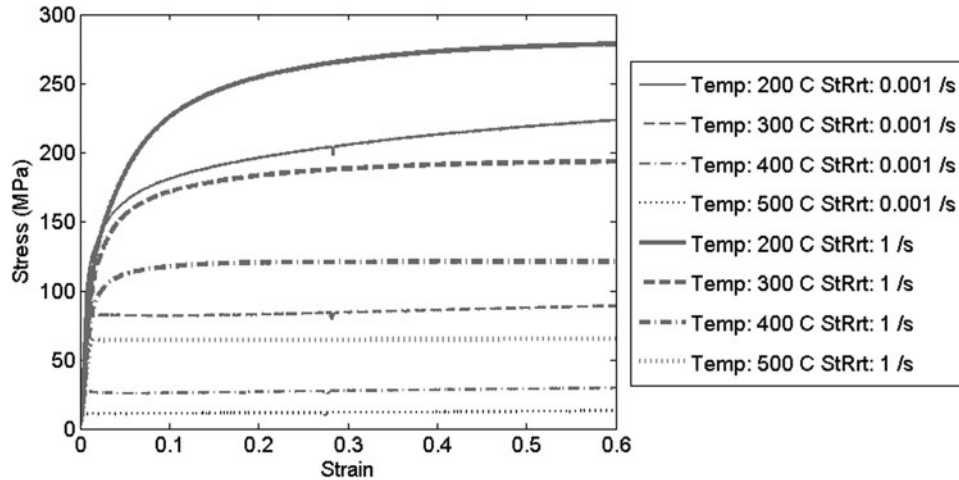


Fig. 2. 5182 Al stress-strain curves for various temperatures and strain rates.

where c^s and σ_o^s are, respectively, the climb tensor and a critical stress associated with climb in the system(s), and n_c is the stress exponent associated with climb. In Eq. (8), n_g and τ_o^s (glide stress exponent and critical resolved shear stress associated with glide) are temperature, strain-rate, and microstructure-dependent [24]. Likewise, n_c and σ_o^s (climb stress exponent and critical stress associated with climb) are dependent of the same variables. This latter dependency however, is much more complex due to the dynamics and interactions of dislocations and the interactions between point defects and dislocations. Additional versions of the VPSC code, including an improved C&G model [25] and an atomistic scale coupled model, are currently being developed and will be added to future analysis.

5. Application of the VPSC Code to 5182 Aluminum Alloy

Experiments performed on 5182 aluminum samples with an initial (001) (“cube”) texture deformed in compression have been reported in Stout et al. [26, 27]. Stress–strain curves and final textures (in terms of inverse pole figures) are measured for varying levels of the two control parameters: temperature and strain rate (Table 1). The experiments are performed until the specimens reach a true strain of 0.6. Final textures are also available for 7 of the 11 stress–strain curves shown in Figure 2.

The stress corresponding to the maximum measured strain of 0.6 and the intensities of the textures corresponding to the (001) and (101) corners of the inverse pole figure are extracted as low-dimensional data for the calibration of the VPSC model. Although a complete, quantitative description of crystallographic textures requires, in general, a large number of parameters (e.g., weights associated with a partition of a 3D orientation space), the final compression textures of the 5182 Al samples can be characterized by, at most, two components with associated intensities, corresponding to a retained (001) cube texture and/or a (101) compression texture. These chosen features offer a low-dimensional yet highly informative metric for model calibration.

5.1. Experimental Observations

The initial results by Stout et al. [26] show typical stress–strain behaviors, in which yielding is followed by strain-hardening at low temperatures. At higher temperatures, however, very little work hardening and lower yield stresses are observed. Additionally, for yield stresses below 50 MPa, negative work hardening occurs with a clear upper/lower yield point; for stresses above 50 MPa, a yield point is not observable, however [26]. Textures at elevated temperatures are likewise inconsistent with standard glide-only deformation textures, while textures at lower temperatures develop a (101) fiber texture, typical of uniaxial compression applied to a FCC polycrystal. Experiments run at 500 and 550°C with a strain rate of 10^{-3} s^{-1} display a (001) cube component (generally thought of as a recrystallization texture not a deformation texture) and almost no (101) deformation component. For 400, 500, and 550°C with 1 s^{-1} strain-rate, both (001) and (101) textures are observed [27]. To explain the difference in the combination of textures, Stout et al. [27] assumes a sharp decrease in rate sensitivity as strain rate increases.

5.2. Prior Work

Utilizing the VPSC model to predict texture measurements reported by Stout et al. [27], Lebensohn et al. [24] observes that the (001) cube component at high temperatures and low strain

Table 2. Control and uncertain model parameter values

	Parameter	Minimum	Maximum
Control parameters	Temperature (°C)	180	570
	Strain-rate (s^{-1})	0.0005	1.05
Uncertain model parameters	n_g	1	5
	τ_o^s (MPa)	1.2	1343.4
	n_c	1	5
	σ_o^s (MPa)	1.2	6045.4

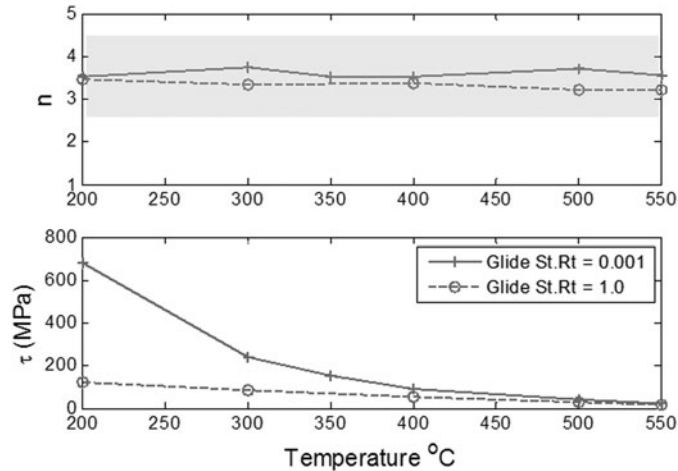


Fig. 3. Optimized point estimates for rate sensitivity (n_g) (top) and critical stress (τ_0) (bottom) for the G model.

rates are due to an increase in climb activity. Seven different VPSC simulations of texture evolution are computed for various glide-only and climb-and-glide scenarios. An analysis of these simulations shows that an increase in rate-sensitivity contributes to prevalence of the (001) cube component. The texture simulated using an equal climb-to-glide activity ratio most accurately predicts the experimental texture for the 400°C and 10^{-3} s^{-1} experimental case, however. As proposed in Lebensohn et al. [24], the final retained (001) cube component is achieved by means of an increase in climb activity, which can be explained by climb mechanism accommodating plastic deformation applied to a single crystal involving a reduced plastic spin (crystal rotation) as compared with glide (see Lebensohn et al. [24] for details). Hereafter, the response features of interest (stress at the maximum measured strain of 0.6, (001) cube texture, and (101) compression texture) will be

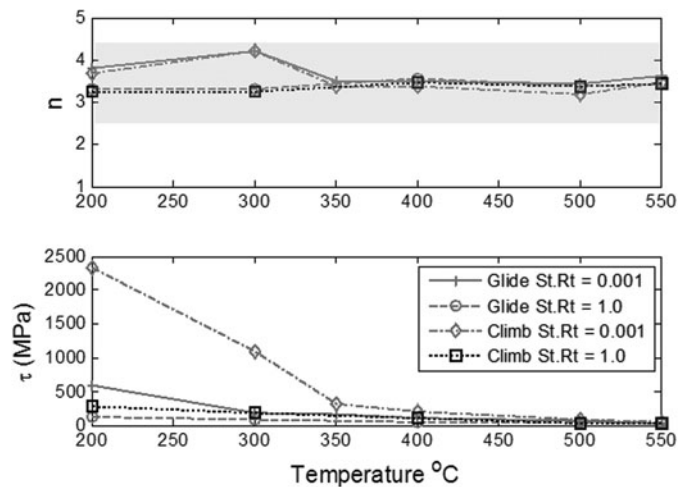


Fig. 4. Optimized point estimates for rate sensitivities (n_g and n_c) (top) and critical stresses (τ_0 and σ_0) (bottom) for the C&G model.

Table 3. Calibration parameters for the G model

Parameter	Optimized/mean value	Min	Max
a_g	4577.1	3432.8	5721.4
b_g	-0.01	-0.008	-0.012
c_g	372.48	279.36	465.60
d_g	-0.005	-0.004	-0.006
n_g	3.5	2.5	4.5

referred to as maximum stress, texture 001, and texture 101, respectively.

6. Calibration Against Experimental Data

The critical stresses and the stress exponents from Eqs. (7) and (8) are uncertain and, thus, will be calibrated against experimental data. As the initial strain hardening is not of interest, the critical stresses are assumed constant. For the G model, the two parameters that need to be calibrated are then (i) the glide stress exponent, n_g , and (ii) the initial critical resolved shear stress for glide, τ_0^s . For the C&G model, in addition to the two parameters corresponding to the glide mechanism, parameters that need calibration include two more parameters: (iii) the climb stress exponent, n_c , and (iv) critical stress associated with climb, σ_0^s . The plausible upper and lower limits for these uncertain parameters are determined by expert opinion and are listed in Table 2.

6.1. Correlation Function

There is a potential dependency of the stress exponent(s), n , and initial critical shear stress(es), τ , on the control parameters (temperature and strain rate) making it implausible to search for a single set of input parameter values for stress exponent and critical stress that can yield satisfactory agreement with experiments throughout the entire domain of applicability. Therefore, it becomes necessary to construct a correlation function to investigate and if present represent the dependency of these uncertain input parameters on control parameters.

Table 4. Calibration parameters for the C&G model

Parameter	Optimized/mean value	Min	Max
a_g	2970.2	2227.65	3712.75
b_g	-0.008	-0.0064	-0.0096
c_g	281.7	211.275	352.125
d_g	-0.004	-0.0032	-0.0048
n_g	3.5	2.5	4.5
a_c	24,727	18,545.25	30,908.75
b_c	-0.012	-0.0096	-0.0144
c_c	1595.2	1196.4	1994
d_c	-0.008	-0.0064	-0.0096
n_c	3.5	2.5	4.5

Table 5. Calibration experiments used in each case (see Table 1 for the experimental settings)

Case	Experiments
1	A
2	A,B
3	A,B,C
4	A,B,C,E
5	A,B,C,E,I
6	A,B,C,E,I,J
7	A,B,C,E,I,J,K
8	A,B,C,E,I,J,K,D
9	A,B,C,E,I,J,K,D,E
10	A,B,C,E,I,J,K,D,E,G
11	A,B,C,E,I,J,K,D,E,G,H

Such a function can be constructed by exploiting the available experimental data.

Optimal values for stress exponent, n , and critical stress, τ , are obtained by minimizing the disagreement between the measured stress and texture values using a nonlinear constrained optimization algorithm, exploiting the experimental measurements available at settings given in Table 1. Sequential quadratic programming (SQP) through the `fmincon` command in MATLAB is implemented [28, 29] (also see [30] for a complete description of the gradient-based SQP algorithm).

$$\tau_{\min} = \frac{0.5 \times \sigma^e}{3 \times \dot{\epsilon}^{(1/3.5)}}, \quad (9)$$

$$\tau_{0\max}^s = \frac{2.0 \times \sigma^e}{3 \times \dot{\epsilon}^{(1/3.5)}}, \quad (10)$$

where σ^e represents the stress at the maximum measured strain. When the range identified for these parameters is normalized between 0 and 1, the starting value for the critical stress is set to 0.33.

For optimization of the C&G model, the stress exponents are allowed to vary between 1.5 and 4.5 with the same starting values as the G model. The bounds on the critical stress associated with glide and the lower bound of the critical stress associated with climb are determined according to Eqs. (9) and (10). The upper bound of the critical stress associated with climb is determined from Eq. (11):

$$\sigma_{0\max}^s = \frac{9.0 \times \sigma^e}{3 \times \dot{\epsilon}^{(1/3.5)}}. \quad (11)$$

When the range identified for these parameters is normalized between 0 and 1, the starting value for the critical stress associated with glide is 0.4 and the initial critical stress associated with climb is 0.9.

The function to be minimized is given by the least-squares objective function in Eq. (12):

$$O = \sqrt{\left(\frac{|\sigma^s(n, \tau) - \sigma^e|}{\sigma^e}\right)^2 + \left(\frac{|\psi(n, \tau)_{(001)}^s - \psi_{(001)}^e|}{\psi_{(001)}^e}\right)^2 + \left(\frac{|\psi(n, \tau)_{(101)}^s - \psi_{(101)}^e|}{\psi_{(101)}^e}\right)^2}, \quad (12)$$

In optimization of the G model, the stress exponents are allowed to vary between 1 and 5, with starting values of 3 and 3.3 for the glide and climb stress exponents, respectively. The lower bound and upper bound of the range for the critical stresses corresponding to the settings of each experimental measurement are determined using Eq. (9) and Eq. (10), respectively.

where σ^s represents the predicted stress at the maximum measured strain. In Eq. (12), $\psi_{(001)}^e$ and $\psi(n, \tau)_{(001)}^s$ denote the measured and predicted texture 001 intensities, respectively; while $\psi_{(101)}^e$ and $\psi(n, \tau)_{(101)}^s$ represent the measured and predicted texture 101 intensities, respectively. Note that for each experimental setting given in Table 1, the $\psi_{(001)}^e$ and $\psi_{(101)}^e$ values are given as ranges due to the experimental uncertainty. Therefore, the following relationships are imposed on the

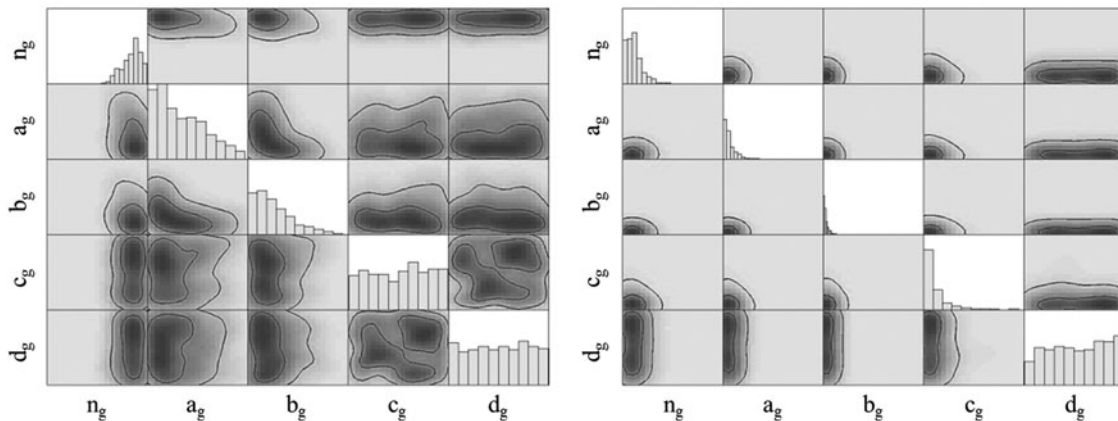


Fig. 5. Posterior distribution for the G model (Left: 1 experiment, Right: 11 experiments) (Inner contour: 90th percentile, Outer contour: 50th percentile).

second and third terms in Eq. (12):

$$\left(\frac{|\psi^s - \psi^e|}{\psi^e}\right)^2 = 0 \text{ for } (\psi^e)_L \leq \psi^s \leq (\psi^e)_U, \quad (13)$$

$$\left(\frac{|\psi^s - \psi^e|}{\psi^e}\right)^2 = \left(\frac{|\psi^s - (\psi^e)_L|}{(\psi^e)_L}\right)^2 \text{ for } \psi^s < (\psi^e)_L, \quad (14)$$

$$\left(\frac{|\psi^s - \psi^e|}{\psi^e}\right)^2 = \left(\frac{|\psi^s - (\psi^e)_U|}{(\psi^e)_U}\right)^2 \text{ for } \psi^s > (\psi^e)_U. \quad (15)$$

In Eqs. (13)–(15), the subscripts U and L denote the upper and lower bounds for texture data from Table 1. Because increased stress leads to an increase in glide at the expense of climb, the constraint $n_c < n_g$ is imposed for all control parameter settings.

Representative plots of the optimized, deterministic point estimates for stress exponent(s) and critical stress(es) are plotted in Figures 3 and 4 for G and C&G models, respectively. In these figures, the starting values are 3 and 3.3 for the glide and climb stress exponents, respectively. Other starting values between 1.8 and 4.2 for the G model and between 2.1

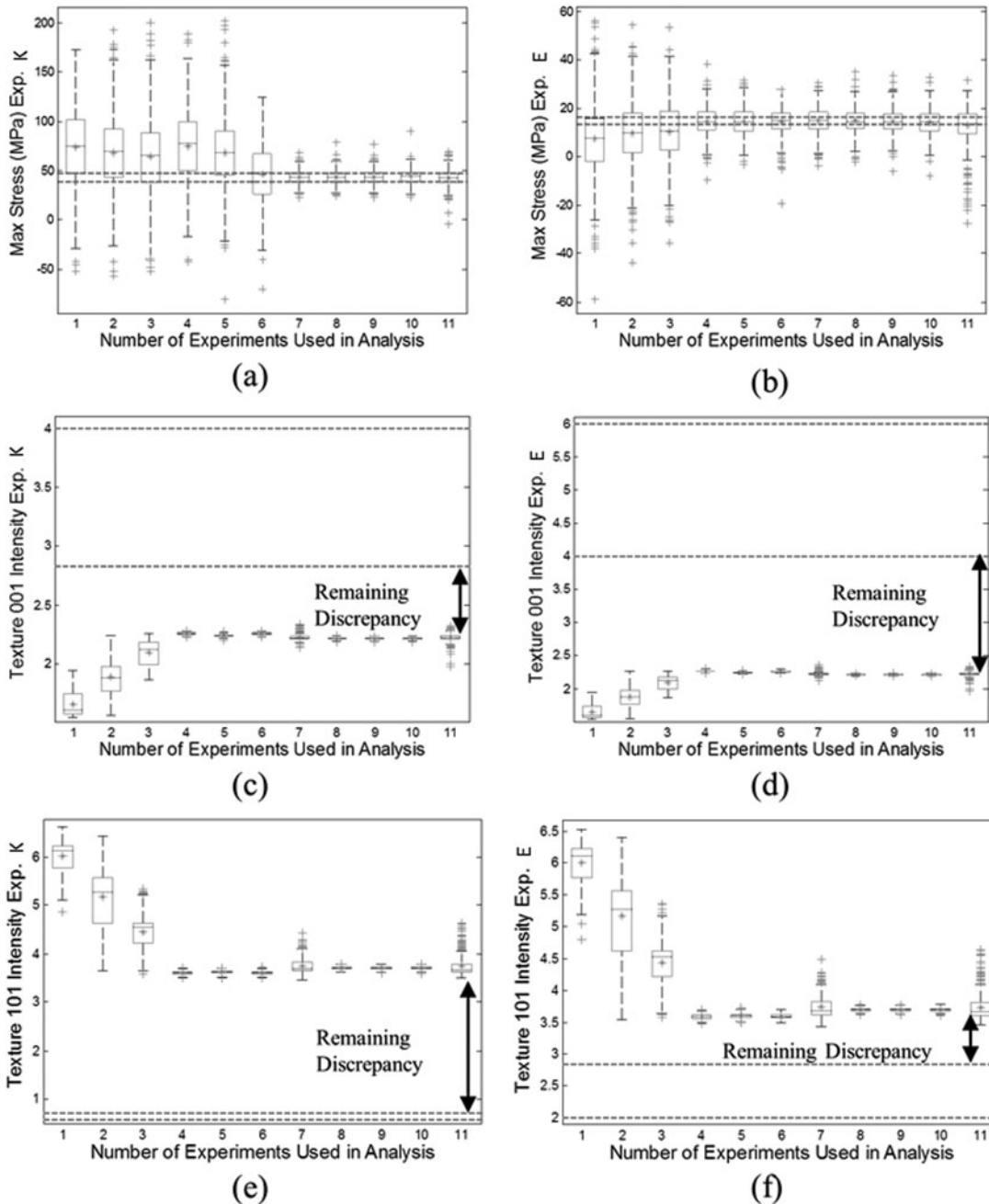


Fig. 6. Model prediction bias and uncertainty for the G model (Left: Experiment K, Right: Experiment E).

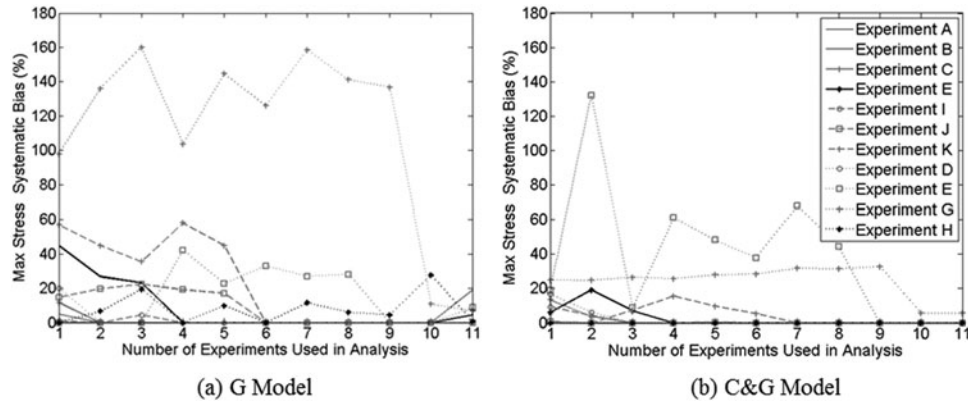


Fig. 7. Systematic bias corresponding to maximum stress for each experiment: (a) G model, (b) C&G model.

and 3.9 for the C&G model yield similar results, demonstrating that the optimized stress exponent(s), n , are independent of temperature and strain rate and, thus, must be treated as calibration parameters. Furthermore, the optimization process indicates that bounds for the stress exponents can be restricted further (see the gray band on Figures 3 and 4) from the ranges identified by the expert (recall Table 2). The further constrained ranges for the stress exponents are listed in Tables 3 and 4.

On the other hand, the optimized critical stress, τ , exhibits an exponential relationship with temperature and a linear relationship with strain rate, which can be expressed as:

$$\tau = ae^{bT} + \frac{(\dot{\epsilon} - \dot{\epsilon}_1) ce^{dT} - (\dot{\epsilon} - \dot{\epsilon}_1) ae^{bT}}{(\dot{\epsilon}_2 - \dot{\epsilon}_1)}, \quad (16)$$

where $\dot{\epsilon}$ is the strain rate and T is the temperature. The variables a and c are the leading intercept coefficients for the exponential fit for the critical stress at a strain rate of $\dot{\epsilon}_1 = 0.001$ and $\dot{\epsilon}_2 = 1$, respectively. Likewise, b and d are the decay rate coefficients for the exponential fit. In lieu of critical stresses, the coefficients a , b , c , and d are treated as calibration parameters, for which posterior distributions are inferred. The optimal values for the coefficients computed from Eq. (12)

and shown in Tables 3 and 4 for the two models, are treated as starting values during model calibration (discussed in the next section).

The aforementioned analysis yields 5 calibration parameters for the G model and 10 for the C&G model as listed in Tables 3 and 4, along with the ranges, within which these parameters are allowed to vary to encompass available experimental data.

6.2. Model Calibration

Latin-hypercube designs with 140 and 240 samples are used to construct the GP emulators for the model predictions of the G model and the C&G model, respectively. For the calibration parameters, a uniform prior distribution is assumed between the ranges given in Tables 3 and 4. Further, 10,000 accepted MCMC iterations are generated to estimate the posterior distribution of the calibration parameters. Exercising the GP emulators, predictions are obtained for 500 linearly spaced samples from the posterior distributions of the calibration parameters and GP hyper-parameters. To compare the calibrated model predictions against experimental data, predictions, $\eta(x, \theta)$, are generated at experimental settings shown in Table 1.

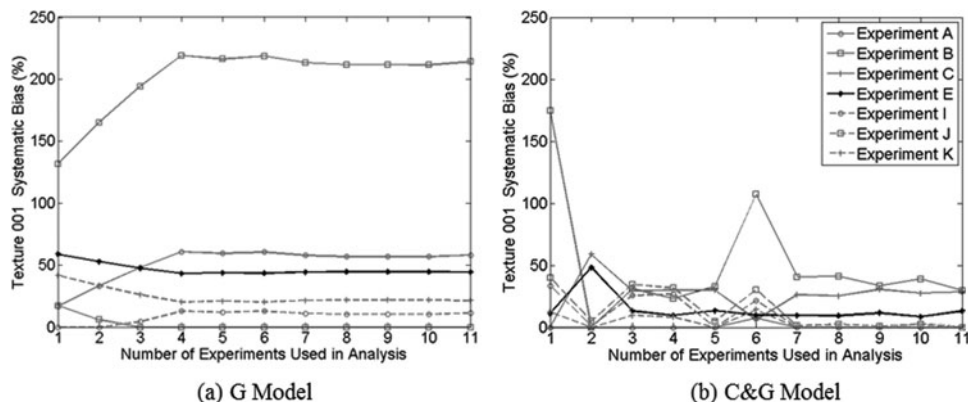


Fig. 8. Systematic bias corresponding to texture 001 for each experiment: (a) G model, (b) C&G model.

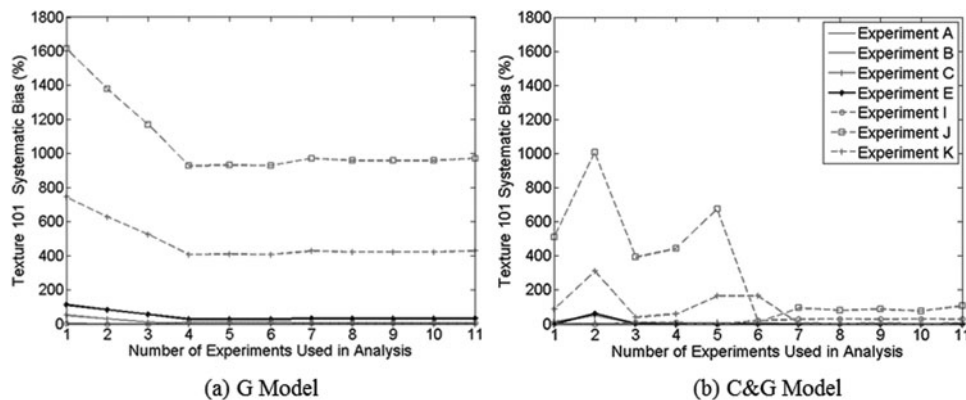


Fig. 9. Systematic bias corresponding to texture 101 for each experiment: (a) G model, (b) C&G model.

7. Results and Discussion

This section demonstrates the resource allocation framework and provides a discussion on the computed systematic bias and information gain as the two versions of the VPSC model are calibrated using one through 11 available experiments in the sequence shown in Table 5. When all 11 experiments are used, coverage of the domain reaches over 85% according to the coverage metric proposed in Hemez et al. [17]. It is assumed that the minimum coverage threshold is set at 80% for this application; therefore, the 11 experiments satisfactorily explore the domain of applicability. The calibrated VPSC models are executed to predict maximum stress along with texture 001 and 101 intensities at the settings of these 11 experiments. This section ultimately concludes by comparing the tradeoff

of bias and uncertainty reduction between the two models through divergence information criterion.

7.1. Initial Numerical Model: G Model

A reduction in uncertainty in the calibration parameters of the G model can be observed by the narrowing of the distributions in Figure 5, which compares the posterior distributions of input parameters obtained using all 11 experiments to those obtained using only one experiment (with the exception of d_g , which can be explained by the relative insensitivity of this parameter). In Figure 6, the stress and texture predictions depict convergent behavior with consistently reduced uncertainty as the number of experiments used in the analysis increases. Also evident in Figure 6 is the constant systematic bias remaining

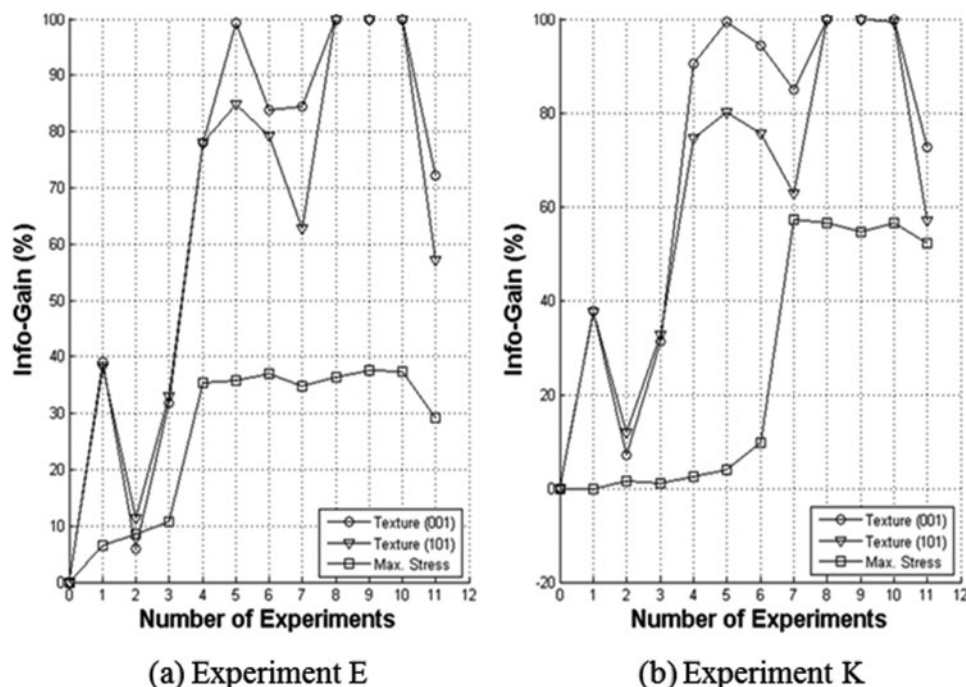


Fig. 10. Information gain from experiments used for calibration of G model: (a) Experiment E, (b) Experiment K.

after the convergence of predictions. The remaining systematic bias is measured to the nearest dashed horizontal line, which reflects the experimental uncertainty.

Figures 7a–9a depict the prediction bias for the maximum stress, texture 001, and texture 101 predictions at each experimental setting, as a function of the number of experiments used in the calibration process. For the maximum stress output shown in Figure 7a, little convergent behavior is evident; while for the texture outputs, upon addition of the fourth

experiment, the inferred prediction bias of the textures converges for all prediction settings, as shown in Figures 8a and 9a.

The information gain is also computed for the model predictions at all experimental settings (recall Table 5). For brevity, however, Figure 10 shows the information gain plots for the maximum stress, texture 001, and texture 101 predictions at settings E and K, respectively. The remaining experimental settings show similar trends. For stress

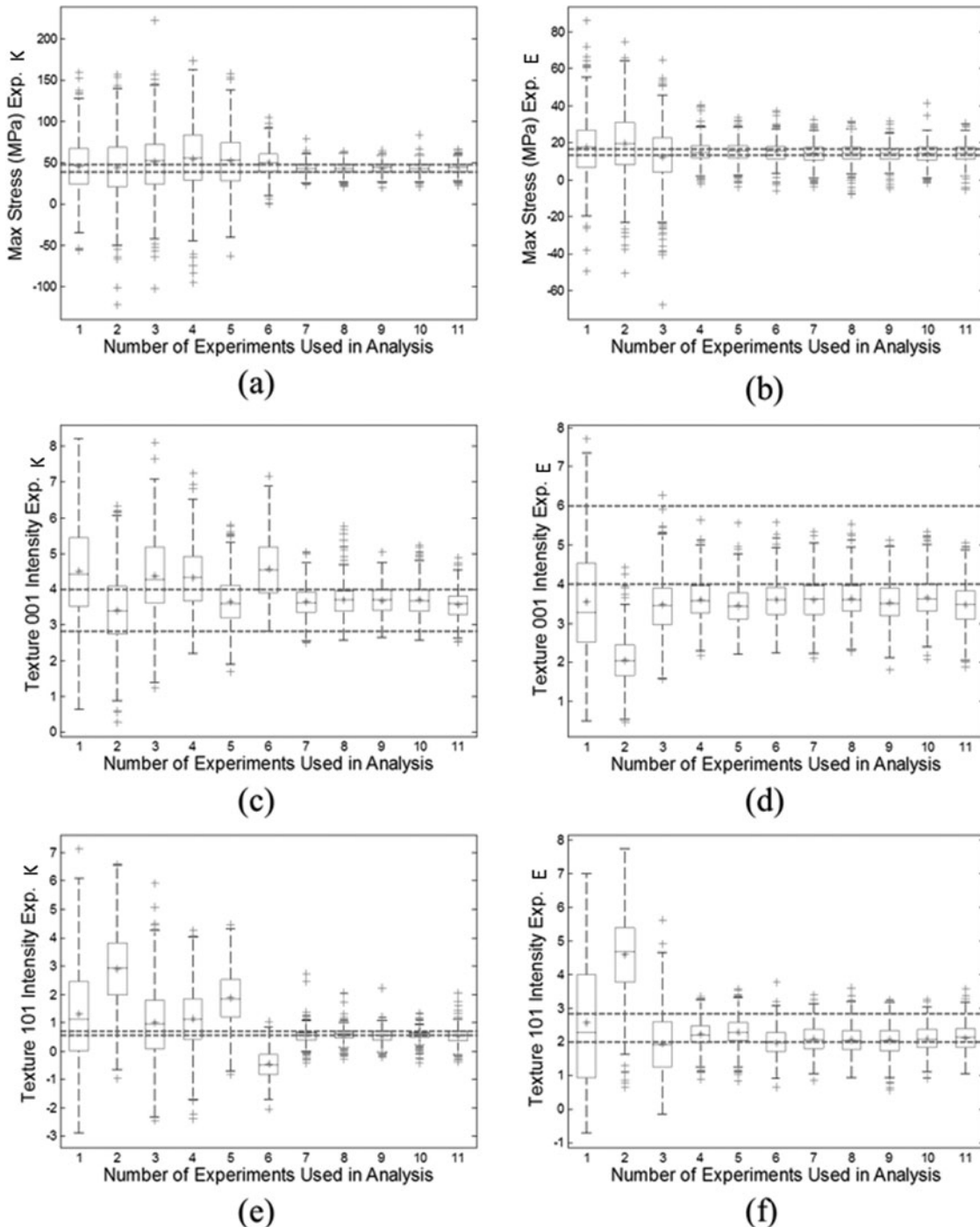


Fig. 11. Model prediction bias and uncertainty for the C&G model (Left: Experiment K, Right: Experiment E).

predictions, the information gain monotonically increases and ultimately converges. Slight fluctuations are expected given the stochastic nature of the inference approach. For the texture predictions, a convergent behavior is not observed, indicating the G model's inability to reproduce texture experiments at certain regions in the domain of applicability. Furthermore, Figures 8 and 9 depict a prediction bias well in excess of 100% for the texture predictions demonstrating that uncertainty reduction alone is insufficient to warrant accurate predictions. In fact, Figure 9 reveals a systematic bias for texture 101 over 400% for setting K, and as high as 1000% for setting J.

Referring back to Figure 1, the G model's systematic bias is unacceptably high. The resource allocation framework then suggests that the rigor in which the physics principles are modeled must be improved, which leads to the C&G model.

7.2. Improved Numerical Model: C&G Model

In Figure 11, it can be observed that the uncertainties in stress and texture predictions of the C&G model reduce and the prediction bias converges to a constant value as the number of experiments available for model calibration increases. Comparing Figures 6 and 11, the more sophisticated, C&G model has significantly less prediction bias compared to the G model. However, the C&G model requires an increased number of experiments to reach convergence. For the C&G model, from Figures 8 and 9, seven experiments are necessary for the prediction bias of the texture to converge; while convergence is achieved with only four experiments for the G model. An increased need for experiments to mitigate parameter uncertainty is expected for the C&G model, which has twice as many calibration parameters as the G model (see Tables 3 and 4).

Figure 12 shows the convergence of information gain after a sufficient number of experiments are used in the calibra-

tion process for experimental settings E and K. Note that since information gain is calculated with respect to the initial uncertainty in input parameters, the specific level of information gain, at which convergence is achieved, is irrelevant. The convergence of both the systematic bias and information gain indicates that prediction uncertainty is remedied. For the C&G model, the systematic bias converges to below 10% for the maximum stress prediction and below 50% for the texture predictions. Should this level of systematic bias be deemed acceptable for the intended purposes, the model may be considered validated, as the coverage exceeds the minimum coverage threshold. If additional reduction in systematic bias is required, however, a further physics sophistication of the model should be considered.

7.3. A Comparative Analysis: Divergence Information Criterion

In summary, according to the framework presented herein, the C&G is the preferred model for making predictions, as the G model is not validated. The lower converged discrepancy of the C&G model confirms that reduction in systematic bias can be achieved through physics sophistication of the code. However, note that due to increased complexity and a larger number of calibration parameters, the C&G model requires more experiments to reach convergence. Therefore, earlier discussion on the calibration of G and C&G models reveals a trade-off relationship between the prediction uncertainty and bias. Provided that both models are validated, preference of one model or the other can be reversed depending on the available experimental data. This section demonstrates this concept on the G and C&G models using the divergence information criterion (DIC), a statistical metric for evaluating preferable models [31].

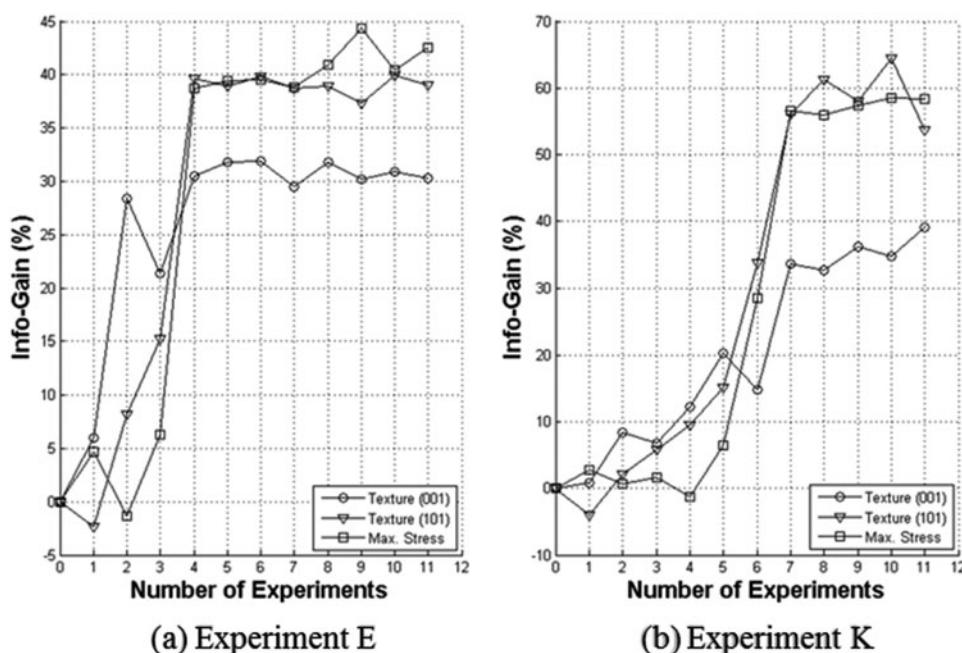


Fig. 12. Information gain from experiments used for calibration of C&G model: (a) Experiment E, (b) Experiment K.

The DIC operates on the model input parameters and their distributions to create a metric that rewards a model for predicting closer to the experiments and penalizes a model for having a larger effective number of parameters. The DIC is computed according to Eqs. (17)–(19):

$$\tilde{p}_j = -2 \int \log[f^{(j)}(y|\theta^{(j)})] \pi^{(j)}(\theta^{(j)}|y) d\theta^{(j)} + 2 \log[f^{(j)}(y|\tilde{\theta}^{(j)}(y))], \quad (17)$$

$$D_j(\theta^{(j)}) = -2 \log[f^{(j)}(y|\theta^{(j)})] + 2 \log[g^{(j)}(y)], \quad (18)$$

$$DIC = D_j(\tilde{\theta}^{(j)}) + 2\tilde{p}_j. \quad (19)$$

In Eq. (17), \tilde{p}_j is the proposed number of effective model parameters, $f^{(j)}(y|\theta^{(j)})$ represents the probability density function for the experimental data y for a given θ for the j th model, $\pi^{(j)}$ represents the prior distribution of emulator parameters, and $\tilde{\theta}^{(j)}(y)$ estimates $\theta^{(j)}$ based upon the experimental data y [32]. In Eq. (18), $2 \log[g^{(j)}(y)]$ is a standardizing term dependent on the observed data. In Eq. (19), \tilde{p}_j represents \tilde{p}_j when $\tilde{\theta}^{(j)}(y)$ is equal to the posterior mean $\tilde{\theta}^{(j)}$. When comparing two models, a smaller value for DIC indicates a preferable model. As the DIC is used for comparison purposes only, the actual DIC values are only relevant relative to another model.

Figure 13 plots the DIC values computed for G and C&G models for an increasing number of experiments. Until the fourth experiment, the less sophisticated G model has a lower DIC value and, thus, the prediction bias outweighs the uncertainty in the parameters. If more than four experiments are available, however, then the C&G model yields a smaller DIC value than that of the G model indicating that the lower prediction bias of the C&G model outweighs the penalty in higher prediction uncertainty due to a larger number of parameters.

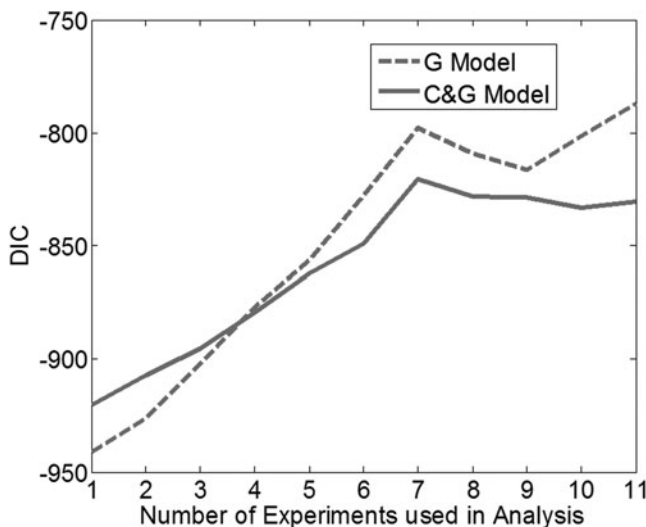


Fig. 13. DIC comparison of the G and C&G models with varying levels of experimental data.

8. Conclusions

It is a routine practice that numerical models are being validated against experiments [33, 34]. In this article, we present a framework to guide the allocation of resources for the validation of numerical models. Improvement in the predictive capabilities of a numerical model can be achieved through the reduction of prediction uncertainty and bias. The prediction uncertainty can be reduced through calibration of model parameters against experimental data. An increase in the number of experiments used in the model calibration results in a decrease in prediction uncertainty, indicated by the convergence of the information gain to a stable level throughout the domain resulting in diminishing returns from additional experiments. In this case, improvements to predictive capabilities are only possible by reducing prediction bias, which can be achieved by improving the physics and/or engineering principles of the given model.

The proposed framework is demonstrated on a nontrivial application of the VPSC code to predict stress and texture behavior of 5182 aluminum alloy. The availability of two versions of the VPSC code, G and C&G models, presents a unique opportunity to demonstrate the fundamental concepts behind the proposed resource allocation framework. In this example, for the G model, the systematic bias of the texture predictions converges while the systematic bias of the stress predictions fails to converge as more experimental data is utilized in the calibration process. The analysis of the information gain shows that parameter uncertainty cannot be further reduced. As the prediction bias for stress fails to converge and the prediction bias for texture converges to an unacceptably high value, the C&G model, with an improved constitutive law, is employed. The convergence of the systematic bias and information gain of the C&G model is observed as the number of experiments available for model calibration increases. The prediction bias of the more sophisticated C&G model converges to a smaller value than that of the G model, but requires a higher number of experiments for convergence, demonstrating the trade-off between reducing prediction bias and uncertainty in model validation. The logical thought process of the proposed framework can provide a science-based, quantifiable, and defensible rationale for allocating resources between code development and experimentation to reduce both uncertainty and bias in the predictions of complex numerical models.

Acknowledgments

The editorial assistance of Godfrey Kimball of Clemson University is gratefully acknowledged. Thanks to Karma Yonten, a former post-doctoral fellow at Clemson University, for his assistance during the preparation of the manuscript.

Funding

This research was performed using funding received from the DOE Office of Nuclear Energy’s Nuclear Energy University Programs (Contract No. 00101999).

References

- [1] M.A. Christie, J. Glimm, J.W. Grove, D.M. Higdon, D.H. Sharp, and M.M. Wood-Schultz, Error analysis and simulations of complex phenomena, *Los Alamos Sci.*, vol. 29, pp. 6–25, 2005.
- [2] T.G. Trucano, L.P. Swiler, T. Igusa, W.L. Oberkamp, and M. Pilch, Calibration, validation, and sensitivity analysis: What's what, *Reliab. Eng. Syst. Saf.*, vol. 91, pp. 1331–1357, 2006.
- [3] S. Atamturktur, F. Hemez, B. Williams, C. Tome, and C. Unal, A forecasting metric for predictive modeling, *Comput. Struct.*, vol. 98, pp. 2377–2387, 2011.
- [4] D. Draper, Assessment and propagation of model uncertainty, *J. R. Stat. Soc.*, vol. 57, pp. 45–97, 1995.
- [5] D. Higdon, J. Gattiker, B. Williams, and M. Rightley, Computer model calibration using high-dimensional output, *J. Am. Stat. Assoc.*, vol. 103, no. 482, pp. 570–583, 2008.
- [6] D. Higdon, C. Nakhleh, J. Gattiker, and B. Williams, A Bayesian calibration approach to the thermal problem, *Comput. Methods Appl. Mech. Eng.*, vol. 197, no. 29–32, pp. 2431–2441, 2008.
- [7] M. Kennedy and A. O'Hagan, Bayesian calibration of computer models (with discussion), *J. R. Stat. Soc., Ser. B*, vol. 68, pp. 425–464, 2001.
- [8] K. Van Buren and S. Atamturktur, A comparative study: Predictive modeling of wind turbine blades, *J. Wind Eng.*, vol. 36, no. 3, pp. 235–250, 2012.
- [9] I. Farajpour and S. Atamturktur, Error and uncertainty analysis of inexact and imprecise computer models, *J. Comput. Civil Eng.*, vol. 27, no. 4, pp. 407–418, 2013.
- [10] J.E. Mottershead and M.I. Friswell, Model updating in structural dynamics: A Survey, *J. Sound Vib.*, vol. 167, no. 2, pp. 347–375, 1993.
- [11] F. Hemez and J. Kamm, Computational methods in transport: Verification and validation, *Lect. Notes Comput. Sci. Eng.*, vol. 62, pp. 229–250, 2008.
- [12] M. Mollineaux, K. Van Buren, F. Hemez, and S. Atamturktur, Simulating the dynamics of wind turbine blades: Part I, model development and verification, *Wind Energy (Wiley)*, vol. 16, no. 5, pp. 694–710, 2013.
- [13] W.L. Oberkamp, T.G. Trucano, and C. Hirsch, Verification, validation, and predictive capability in computational engineering and physics, Report SAND2003-3769, Sandia National Laboratories, Albuquerque, NM, 2003.
- [14] B.H. Thacker, S.W. Doebeling, F.M. Hemez, M.C. Anderson, J.E. Pepin, and E.A. Rodriguez, Concepts of model verification and validation, Report LA-14167-MS, Los Alamos National Laboratories, Los Alamos, NM, 2004.
- [15] D.E. Thompson, K.B. McAuley, and P.J. McLellan, Design of optimal experiments to improve model predictions from a polyethylene molecular weight distribution model, *Macromol. React. Eng.*, vol. 4, no. 1, pp. 73–85, 2010.
- [16] S. Atamturktur, M. Egeberg, F. Hemez, and G. Stevens, Defining coverage of an operational domain using a modified nearest-neighbor metric, *Mech. Syst. Signal Pr.*, vol. 50–51, pp. 349–361, 2015.
- [17] F. Hemez, S. Atamturktur, and C. Unal, Defining predictive maturity for validated numerical simulations, *Comput. Struct.*, vol. 88, pp. 497–505, 2010.
- [18] C.J. Stull, F. Hemez, B.J. Williams, C. Unal, and M.L. Rogers, An improved description of predictive maturity for verification and validation activities, Los Alamos National Laboratories Technical Report LA-UR-11-05659, 2011.
- [19] C.E. Shannon, A mathematical theory of communication, *Bell Syst. Tech. J.*, vol. 27, pp. 623–656, 1948.
- [20] W.K. Hastings, Monte Carlo sampling methods using Markov chains and their applications, *Biometrika*, vol. 57, pp. 97–109, 1970.
- [21] N. Metropolis, A.W. Rosenbluth, M.N. Rosenbluth, A.H. Teller, and E. Teller, Equations of state calculations by fast computing machines, *J. Chem. Phys.*, vol. 21, no. 6, pp. 1087–1092, 1953.
- [22] R.A. Lebensohn and C.N. Tomé, A self-consistent anisotropic approach for the simulation of plastic deformation and texture development of polycrystals: Application to zirconium alloys, *Acta Mater.*, vol. 41, no. 9, pp. 2611–2623, 1993.
- [23] R.A. Lebensohn, Y. Liu, and P.P. Castañeda, On the accuracy of the self-consistent approximation for polycrystals: Comparison with full-field numerical simulations, *Acta Mater.*, vol. 52, pp. 5347–5361, 2004.
- [24] R.A. Lebensohn, C.S. Hartley, C.N. Tomé, and O. Castelnau, Modeling the mechanical response of polycrystals deforming by climb and glide, *Philos. Mag.*, vol. 90, no. 5, pp. 567–583, 2010.
- [25] R.A. Lebensohn, R.A. Holt, J.A. Caro, A. Alankar, and C.N. Tomé, Improved constitutive description of single crystal viscoplastic deformation by dislocation climb, *C. R. Mec.*, vol. 340, pp. 289–295, 2012.
- [26] M.G. Stout, S.R. Chen, U.F. Kocks, A.J. Schwartz, S.R. MacEwen, and A.J. Beaudoin, Constitutive modeling of a 5182 aluminum as a function of strain rate and temperature. In: *Hot Deformation of Aluminum Alloys II*, T. Bieler, T.A. Lalli, L.A. MacEwen, Sr., Eds., TMS, Warrendale, PA, vol. 1009, pp. 205–216, 1998.
- [27] M.G. Stout, S.R. Chen, U.F. Kocks, A.J. Schwartz, S.R. MacEwen, and A.J. Beaudoin, Mechanisms responsible for texture development in a 5182 aluminum alloy deformed at elevated temperature. In: *Hot Deformation of Aluminum Alloys II*, T. Bieler, T.A. Lalli, L.A. MacEwen, Sr., Eds., TMS, Warrendale, PA, vol. 1009, pp. 243–254, 1998.
- [28] M.J.D. Powell, A fast algorithm for nonlinearly constrained optimization calculations. In: *Numerical Analysis*, G.A. Watson, Ed., Lecture Notes in Mathematics, Springer Verlag, Berlin, vol. 630, 1978.
- [29] R.A. Waltz, J.L. Morales, J. Nocedal, and D. Orban, An interior algorithm for nonlinear optimization that combines line search and trust region steps, *Math. Program.*, vol. 107, no. 3, pp. 391–408, 2006.
- [30] J. Nocedal and S.J. Wright, *Numerical Optimization*, Second Edition, Springer Series in Operations Research, Springer Verlag, Berlin, 2006.
- [31] D.J. Spiegelhalter, N.G. Best, B.P. Carlin, and A. van der Linde, Bayesian measure of model complexity and fit (with discussion), *J. R. Stat. Soc., Ser. B*, vol. 64, pp. 583–639, 2002.
- [32] B.J. Williams, R. Picard, and L. Swiler, Multiple model inference with application to model selection for the reactor code R7, Report LA-UR-11-05625, Los Alamos National Laboratories, Los Alamos, NM, 2011.
- [33] K. Li, X.-L. Gao, and A.K. Roy, Micromechanical modeling of viscoelastic properties of carbon nanotube-reinforced polymer composites, *Mech. Adv. Mater. Struct.*, vol. 13, no. 4, pp. 317–328, 2006.
- [34] A. El-Sabbagh and A. Baz, A coupled nonlinear model for axisymmetric acoustic resonators driven by piezoelectric bimorphs, *Mech. Adv. Mater. Struct.*, vol. 13, no. 2, pp. 205–217, 2006.